

2

DIFFERENTIATION

In this chapter, we introduce dielectric metasurfaces that perform optical image edge detection in the analog domain using a subwavelength geometry that can be readily integrated with detectors.

The first section will briefly review known notions of Fourier optics defining concepts that are useful throughout the thesis. Next, the idea of using a Fano resonant metasurface as a spatial filter is introduced. Section 2.3 describes how to tailor the spatial dispersion of the metasurface by manipulating its leaky modes dispersion and the related Fano resonance asymmetry and linewidth. In Section 2.4 the optimized transfer functions are used to numerically test how well the ideal 1st- and 2nd-order differentiation are approximated by our realistic metasurface designs.

In Section 2.5 the fabrication process is described step by step both for the metasurface and for the images used as diapositives. Next, the fabrication results are presented and the samples' optical characterization is discussed. In Section 2.6 the optical setups used are described along with the measurements. Finally, the experimental 2nd-order differentiation is compared to its ideal counterpart showing significant agreement. The last section extends these concepts to 2D operations and unpolarized illumination, numerically demonstrating edge-detection regardless of the orientation.

Parts of the calculations supporting this Chapter are presented in Appendix A.

The first part of Section 2.1 dealing with Fourier optics follows the notation and the description of Ref. [1].

2.1. FOURIER OPTICS

AN arbitrary two-dimensional input wave signal (i.e. an image) can be represented in general by a complex function $f(x, y)$. If the latter function is absolutely integrable (i.e. $f \in L^1(\mathbb{R}^2)$) it can be thought as the superposition of spatial harmonic functions of the form

$$F(v_x, v_y) \exp [i2\pi(v_x x + v_y y)] \quad (2.1)$$

where $F(v_x, v_y)$ is a complex amplitude and v_x, v_y are called *spatial frequencies* and define the harmonic functions' periodicities $\Lambda_x = 1/v_x$ and $\Lambda_y = 1/v_y$ along the x and y directions. This concept is intuitively shown in Figure 2.1 and can be rigorously formalized as

$$f(x, y) = \iint_{-\infty}^{\infty} F(v_x, v_y) \exp [i2\pi(v_x x + v_y y)] dv_x dv_y \quad (2.2)$$

where $F(v_x, v_y)$ is the Fourier transform of $f(x, y)$. Next, it is important to show that these harmonic functions can be mapped one-to-one to simple plane waves (see Figure 2.2a). In fact, any arbitrary harmonic function can be seen as a slice of the monochromatic plane wave $U(x, y, z) = A \exp [i(k_x x + k_y y + k_z z)]$, with wavevector $\mathbf{k} = (k_x, k_y, k_z)$, complex amplitude A and wavelength λ , at the plane $z = 0$, provided that $k_x = 2\pi v_x$ and $k_y = 2\pi v_y$. Vice-versa, the knowledge of the spatial frequencies of a harmonic function completely determines the corresponding plane wave as the knowledge of k_x and k_y is sufficient to determine the k_z via the relation $k_x^2 + k_y^2 + k_z^2 = 2\pi/\lambda^2$.

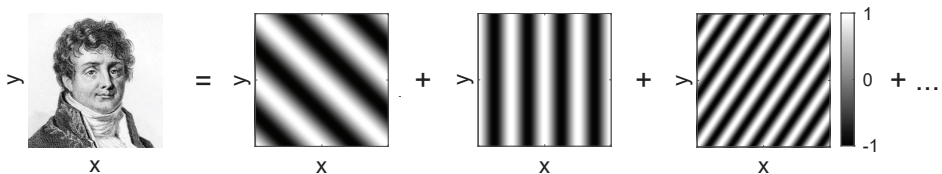


Figure 2.1: An arbitrary image can be expanded into a set of harmonic functions. Here the real part of Eq. (2.1) is plotted for three couples (v_x, v_y) and $F(v_x, v_y) = 1$.

Suppose that a monochromatic plane wave with unit amplitude propagating along the z axis impinges on a thin optical element (e.g. a transparency or a diapositive) with a certain complex transmission function $f(x, y)$. All the harmonic functions composing $f(x, y)$ can be seen as a slice of a corresponding plane wave propagating in a certain direction making angles $\theta_x = \arcsin(\lambda v_x)$ and $\theta_y = \arcsin(\lambda v_y)$ with the y - z and x - z planes, respectively. Hence, as the plane wave is passing through the transparency it is also dispersed into its spatial components and the transmitted wave $U(x, y, z)$ is a superposition of plane waves

$$U(x, y, z) = \iint_{-\infty}^{\infty} F(v_x, v_y) \exp [i2\pi(v_x x + v_y y)] \exp(ik_z z) dv_x dv_y. \quad (2.3)$$

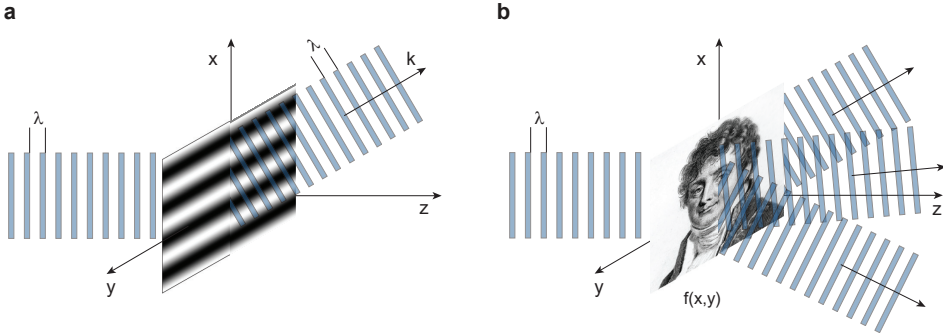


Figure 2.2: **a** A thin optical element that has a complex transmission equal to the harmonic function $\exp[i2\pi\nu_x x]$ bends light at an angle $\theta_x = \arcsin(\lambda\nu_x)$. This is the working principle of a phase grating. **b** The same concept can be extended to an arbitrary complex transmission $f(x, y)$ composed of many harmonic functions.

This bundle of plane waves, schematically illustrated in Figure 2.2b, is the spatial content of the image and contains its information just as $f(x, y)$ does. Manipulating the plane waves composing it is equivalent to performing a certain operation on $f(x, y)$ itself.

The advantage of such theoretical framework becomes clear when dealing with arbitrary traveling waves that are interacting with optical systems. Indeed, if the system response is known for every plane wave composing the arbitrary input signal then the output can be readily calculated. In particular, if the two dimensional optical system relating an input function $f_1(x, y)$ to the output function $f_2(x, y)$ is *linear* and *shift-invariant* (or isoplanatic)¹ then

$$F_2(\nu_x, \nu_y) = H(\nu_x, \nu_y)F_1(\nu_x, \nu_y) \tag{2.4}$$

where $F_1(\nu_x, \nu_y)$ and $F_2(\nu_x, \nu_y)$ are the Fourier transforms of f_1 and f_2 and $H(\nu_x, \nu_y)$ is a function describing the response of the optical system to plane waves called *transfer function*. Intuitively, by modulating its spatial content, $H(\nu_x, \nu_y)$ transforms $f_1(x, y)$ into $f_2(x, y)$.

Among the vast realm of operations, n^{th} -order spatial differentiation is of great appeal in the field of augmented reality and object recognition. In fact, performing the derivative of an image reveals its edges and, in turn, edge detection is a fundamental tool for object recognition. Thus, it is important to assess what transfer function corresponds to the latter operation. Moving to the 1D case, if $f(x)$ is an arbitrary wave input signal, then its n^{th} -order derivative $\frac{d^n f(x)}{dx^n}$ equals $(ik_x)^n F(k_x)$ in the spatial domain, where $F(k_x)$ is the Fourier transform of $f(x)$. Thus, the transfer function corresponding to the n^{th} -order derivative is $H_n(k_x) = (ik_x)^n$.

Proof. $\frac{d^n f(x)}{dx^n} \rightarrow (ik_x)^n F(k_x)$

Suppose $f(x)$ is an arbitrary function $\in L^1(\mathbb{R})$ and let us introduce the notation $\mathcal{F}[f(x)]$

¹A system is said linear if the response to the sum of any linear combination of inputs is the linear combination of the responses to each input. A system is said isoplanatic if a shift to the input function in space corresponds to the same shift in output.

for the Fourier transform of $f(x)$

$$\mathcal{F}[f(x)] = \int_{-\infty}^{\infty} f(x)e^{-ik_x x} dx \quad (2.5)$$

then the transform of the first derivative $f'(x)$ of the function reads

$$\mathcal{F}[f'(x)] = \int_{-\infty}^{\infty} f'(x)e^{-ik_x x} dx. \quad (2.6)$$

This integral can be solved by parts

$$\int_{-\infty}^{\infty} f'(x)e^{-ik_x x} dx = f(x)e^{-ik_x x} \Big|_{-\infty}^{+\infty} + ik_x \int_{-\infty}^{\infty} f(x)e^{-ik_x x} dx \quad (2.7)$$

the first term goes to zero since $f \in L^1(\mathbb{R})$ while the second term is just $\mathcal{F}[f(x)]$. Hence

$$\mathcal{F}[f'(x)] = ik_x \mathcal{F}[f(x)] \quad (2.8)$$

and the transfer function corresponding to 1st-order derivative is $H_1 = ik_x$. Repeating this procedure n times demonstrates the property $\frac{d^n f(x)}{dx^n} \rightarrow (ik_x)^n F(k_x)$. \square

As a consequence, 2nd-order differentiation can be achieved by a metasurface that has a parabolic transfer function that modulates the spatial frequencies composing the input signal [1, 2]. If the metasurface can be treated as a simple two-ports optical system (i.e. no extra diffraction channels are opened other than the 0th-order) then the system's transfer function coincides with the scattering matrix element representing transmission S_{21} (see Appendix A for a brief introduction to the scattering matrix formalism). Hence, from now on, $S_{21}(k_x)$ will be also referred to with the term transfer function. As explained in the next paragraph, we introduce the idea of using a Fano-resonant metasurface to design a specific angular transmission response and therefore $S_{21}(k_x)$.

2.2. FANO RESONANCE

In this work, we design and realize optical metasurfaces composed of dielectric nano-beams that are illuminated by light polarized along the beams' direction. We tailor the spatial dispersion of the metasurfaces by controlling the leaky modes guided along the surface [3–6]. Indeed, when the frequency and in-plane wave vector of incident light match one of these quasi-guided modes, an asymmetric Fano line-shape appears in the transmission spectrum [7–9], due to interference with the broad Fabry-Pérot resonance determined by the thickness and fill fraction of the structure.

Figure 2.3a shows the simulated transmission S_{21} spectra of an array of dielectric nano-beams (width $w = 182$ nm, height $h = 123$ nm, pitch $p = 250$ nm and refractive index $n = 4$ typical for Si) for incident angles ranging from 0 to 0.3 radians ($\sim 17^\circ$). Due to the Fano interference, the transmission swings from 0 to unity within a narrow bandwidth. The sharp response in frequency corresponds to strong non-locality: the spectrum is largely dependent on the incident angle and the transmission minimum shifts

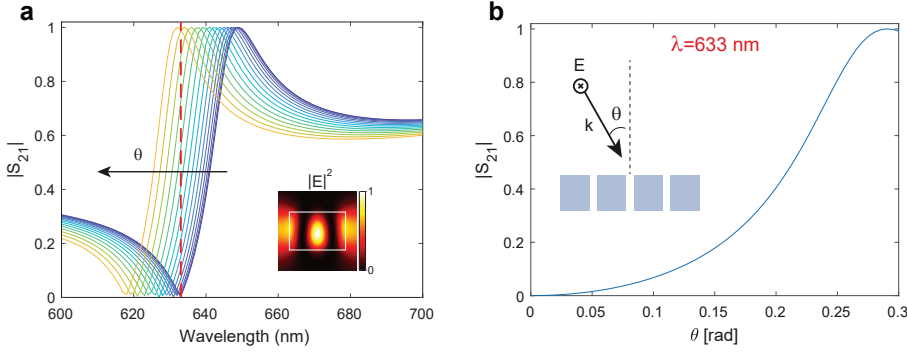


Figure 2.3: **a** Fano-resonant metasurface transmission spectra. Simulated transmission spectra of a metasurface consisting of an array of dielectric nanobeams (width $w = 182$ nm, height $h = 123$ nm, pitch $p = 250$ nm and refractive index $n = 4$) as the incident angle is changed from 0 (blue line) to 0.3 rad (yellow line) in 15 steps. The red dashed line indicates the wavelength of operation ($\lambda = 633$ nm). **b** Cross-cut through panel a showing the transmission at $\lambda = 633$ nm as the incidence angle θ is changed. Insets: electric field amplitude profile within a unit cell at the resonant wavelength; schematic of the proposed structure showing incoming light polarization.

from $\lambda = 633$ nm to $\lambda = 618$ nm over the simulated angular range. The strong amplitude variation in transmission, and the sensitivity to the incoming k -vector, are often undesirable features of resonant metasurfaces, yet here these features enable the use of the metasurface as a Fourier spatial filter, and tailor with large flexibility its angular transmission response and thus transfer function. In fact, by tuning the dispersion of the quasi-guided mode resonance, as well as the Fano line-shape asymmetry and linewidth, it is possible to design an optimized transfer function for a specific excitation wavelength (see Figure 2.3b), as described in the next paragraph.

2.3. DESIGN

The main idea behind our designs of metasurfaces for image processing is that their transfer function can be tuned by introducing a Fano resonance in transmission, and manipulating its dispersion asymmetry and linewidth. In order to prove this property, we use the general formula for a Fano lineshape [8, 10]

$$|S_{21}| = \frac{(\epsilon + q)^2}{\epsilon^2 + 1} m, \quad (2.9)$$

where S_{21} is the scattering matrix element representing transmission for a generic two-port optical system, $m = 1/(1+q^2)$ is a normalization factor, and $\epsilon(k_x) = 2(\omega - \omega_0(k_x))/\Gamma$ is a dimensionless parameter that traces the detuning of the operation frequency ω relative to the resonance at $\omega_0(k_x)$ (dispersing with wavevector k_x), normalized to the linewidth Γ of the resonance. One way to achieve a dispersive resonance frequency is by using one of the leaky-wave resonances of the metasurface. In this case, incident waves are coupled to surface waves propagating along the metasurface through the additional momentum

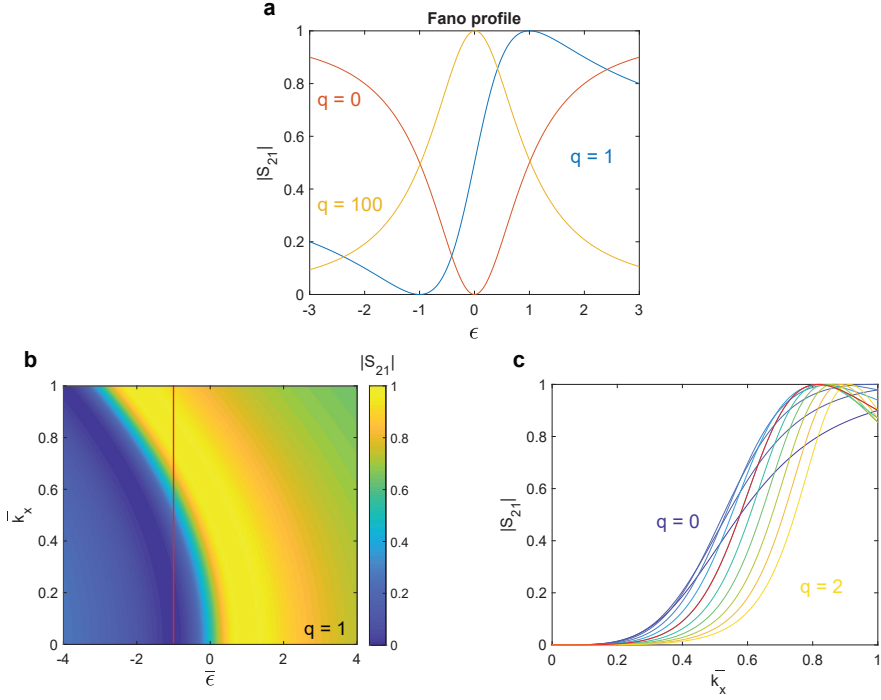


Figure 2.4: **a** Plot of $|S_{21}|$ (from Eq.(2.9)) for $q = 0$ (orange solid line), $q = 1$ (blue solid line), $q = 100$ (yellow solid line). **b** Plot of $|S_{21}|$ (from Eq.(2.9)) as function of $\bar{\epsilon}$ and \bar{k}_x for a parabolic dependence of ω_0 on k_x and fixed values for the shape parameter $q = 1$ and for the linewidth $\Gamma = 1$. **c** Plot of $|S_{21}|$ (from Eq.(2.9)) as a function of \bar{k}_x as q is changed from 0 (blue line) to 2 (yellow line) in steps of 0.2. The red solid line corresponds to the indicated cross-cut through b.

added to them by the metasurface and $\omega_0(k_x)$ generally follows the dispersion of these surface waves. The variable q is a phenomenological lineshape parameter that reflects the contribution of the discrete state in a Fano resonance relative to that of the continuum. Without specifying the nature of the resonance yet we show how it is possible to design the transfer function $|S_{21}(k_x)|$ by tuning the parameters in Eq.(2.9). Starting with q , Figure 2.4a shows how it controls the asymmetry of the Fano lineshape: for $q = 0$ the transmission has a symmetrical dip at the $\bar{\epsilon}$ corresponding to the system resonance; for increasing values of q the lineshape evolves from a completely asymmetric one (data plotted for $q = 1$) to a standard Lorentzian peak (for $q \rightarrow \infty$, data not shown). In the most general case, $\omega_0(k_x)$ can be expressed as $\omega_0(k_x) = \omega_0(0) + \sum_n \alpha_n (\frac{ck_x}{\omega_0(0)})^n$ by applying the Taylor expansion at $k_x = 0$. Note that k_x is normalized versus the free-space wavenumber at $\omega_0(0)$ so that all α_n are expressed in the same frequency units. In reciprocal structures $\omega_0(-k_x) = \omega_0(k_x)$, indicating that all the odd-order terms are zero ($\alpha_1 = \alpha_3 = \dots = 0$). Then, the dominant term in the expansion is the one with $n = 2$, and in Figure 2.4b we plot the transmission as a function of the normalized frequency $\bar{\epsilon} = 2(\omega - \omega_0(0))/\Gamma$ and normalized wavenumber $\bar{k}_x = ck_x/\omega_0(0)$ for fixed values of q and Γ and

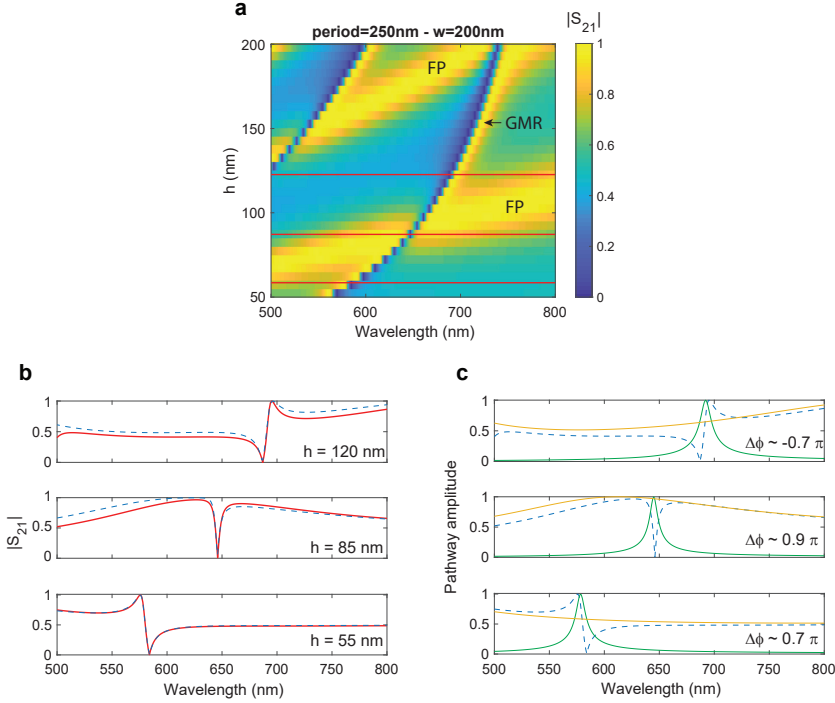


Figure 2.5: **a** Simulated transmission spectra of an array of nanobeams ($n = 4$, $w = 200$ nm, $p = 250$ nm) as the height h is swept from 50 nm to 200 nm. The electric field \mathbf{E} is polarized along the nanobeams. The labels indicate the spectral position of the guided-mode-resonance (GMR) and of the maxima of the Fabry-Pérot background (FP). **b** Cross-cuts through panel a for $h = 55$ nm, $h = 85$ nm and $h = 120$ nm (red solid lines) and fitted spectra according to coupled-mode theory (blue dashed lines). **c** Amplitude of the direct (yellow) and resonant (green) pathways composing the fits (blue dashed lines).

assuming only the second-order dominant term in the Taylor expansion of $\omega_0(k_x)$ with $\alpha_2 = -3/2$. Taking a cross-cut of the data at the $\bar{\epsilon}$ of the minimum for $k_x = 0$ it is possible to study the behavior of $|S_{21}(k_x)|$ as a function of q . As shown in Figure 2.4c, tuning the asymmetry of the Fano lineshape strongly affects the concavity and shape of the transfer function $|S_{21}(k_x)|$. In particular for $q = 1$ a close-to-parabolic shape can be obtained, similar to what is desired for the optimized 2nd-order differentiation. It is important that, in actual realizations, also q and Γ might disperse with k_x but for the sake of simplicity this is not taken into account here.

Next, we discuss how the structural parameters of the metasurface are connected to the variables just described. While there is no trivial way to design $\omega_0(k_x)$, it is straightforward to tune q . Figure 2.5a shows the simulated transmission spectra of an array of nanobeams (refractive index $n = 4$) with fixed width ($w = 200$ nm) and periodicity ($p = 250$ nm) as the height h is swept from 50 nm to 200 nm. It is easy to notice how the asymmetry of the Fano lineshape changes as h is increased (see Figure 2.5b). The Fano lineshapes for this type of metasurfaces are induced by the interference between sharp

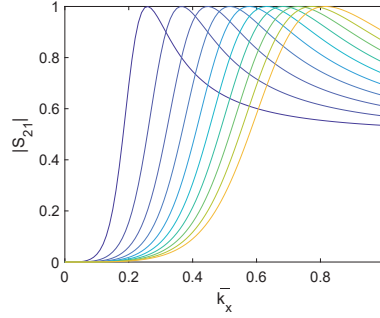


Figure 2.6: Plot of $|S_{21}|$ (from Eq.(2.9)) as function of k_x for a parabolic dependence of ω_0 on k_x with $\alpha_2 = -3/2$ and a fixed shape parameter $q = 1$ as Γ is increased from 0.1 (blue line) to 1 (yellow line) in steps of 0.1.

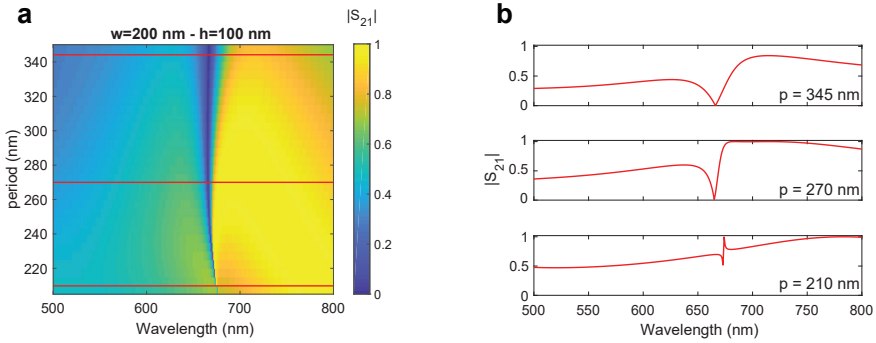


Figure 2.7: **a** Simulated transmission spectra of an array of nanobeams ($n = 4$, $w = 200$ nm, $h = 100$ nm) as the period p is swept from 205 nm to 350 nm. The electric field \mathbf{E} is polarized along the nanobeams. **b** Cross-cuts through panel **a** for $p = 210$ nm, $p = 270$ nm and $p = 345$ nm (red solid lines).

quasi-guided modes that can be launched in-plane along the structure and a broader Fabry-Pérot (FP) background determined by the fill fraction F and the height h of the structure; these two different light pathways correspond to spectral features that are easily distinguishable in Figure 2.5a (see labels). Changing the height of the structure shifts the frequency response of both pathways and thereby controls the amplitude and phase at which they interfere to generate the asymmetric lineshape. This property is formalized in Coupled-Mode Theory (CMT) [11, 12] that provides an analytical form for the transmission of a system with a guided-mode resonance (see Appendix A)

$$S_{21} = t \pm \frac{-(r \pm t)\gamma}{i(\omega - \omega_0) + \gamma}, \quad (2.10)$$

where ω_0 is the resonance frequency, γ is the radiative leakage rate and r and t are the reflection and transmission Fresnel coefficient for a uniform slab of index $n_{\text{eff}} = [(1-F)n_0^2 + Fn^2]^{1/2}$ (with $n = 4$ and $n_0 = 1$) [13]. Thus, the first term in Eq.(2.10) represents the broad FP background while the second term represents the guided-mode-resonant

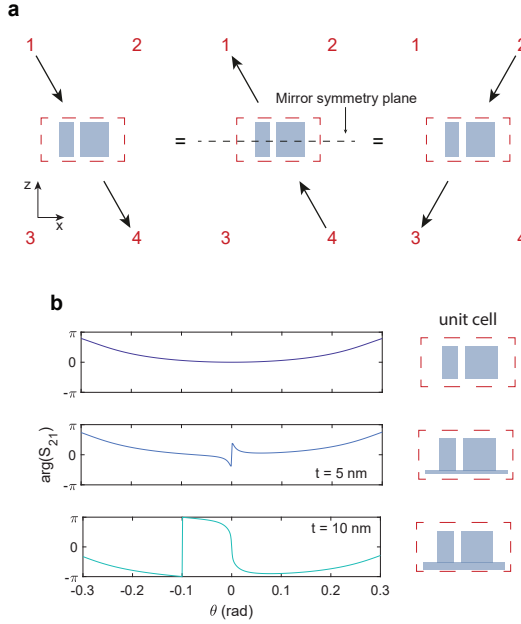


Figure 2.8: **a** The transmission response is still symmetric if only one of the symmetries is broken. **b** Simulated transmission phase of an array of nanobeams ($n = 4$, $w_1 = 40$ nm, $w_2 = 108$ nm, gap between the wires equal to 16 nm, $h = 100$ nm and $p = 250$) as the residual thickness t is increased from 0 to 10 nm to break the vertical symmetry. The electric field \mathbf{E} is polarized along the nanobeams.

pathway. Since these two terms are complex valued it is important to study their phase difference $\Delta\phi = \arg(t) - \arg\left(\pm \frac{-(r \pm t)\gamma}{i(\omega - \omega_0) + \gamma}\right)$ on resonance to understand how the two pathways combine and hence determine the final asymmetry of the Fano resonance. To do this, we fit the simulated transmission of Figure 2.5a for three different heights (see Figure 2.5b–c) using Eq.(2.10). Figure 2.5c shows the amplitude of the two pathways that are composing the fitted functions (dashed blue lines) as well as their phase difference $\Delta\phi$ at the resonance wavelength (inset) highlighting the importance of this phase lag and its influence on the final resonant lineshape. This analysis shows that thickness tuning provides a direct handle on the asymmetry parameter in $|S_{21}|$, which in turn gives control over the curvature of the transfer function around $k_x = 0$.

Next, we assess how to control the numerical aperture of operation. This is directly controllable by the linewidth parameter Γ in Eq.(2.9). Figure 2.6 shows $|S_{21}(k_x)|$ for fixed q and a parabolic $\omega_0(k_x)$ as Γ is increased. As the linewidth of the resonance is increased also the metasurface operational wavevector range is expanded. Hence, Γ allows direct tuning of the metasurface numerical aperture (NA). In simulation, it is possible to tune the linewidth by changing the array periodicity while keeping the nanobeam dimensions fixed, as shown in Figure 2.7a–b. However, an upper bound on periodicity is set by the onset of higher order diffraction channels at large pitches. These would complicate the design of the transfer function and lower the efficiency.

In the case of 1st-order differentiation, not only the amplitude of the transfer function $|S_{21}(k_x)|$, but also the phase $\arg(S_{21}(k_x))$ is important. In fact, such operation requires a response that has odd-symmetry around the sample normal $S_{21}(-k_x) = -S_{21}(k_x)$. In other words, the transmission phase for positive k_x values should be phase-shifted by π compared to that of negative k_x values. In order to achieve this asymmetric phase response, it is necessary to break the unit cell's mirror symmetry both along the propagation (i.e. z -axis) and transverse (i.e. x -axis) directions. Invoking Lorentz reciprocity, it is easy to show that breaking the mirror symmetry only along the x -axis is not sufficient (see Figure 2.8a) to generate a transmission response of odd symmetry. Indeed, the transmission at negative incidence angles (from port 1 to 4) S_{41} has to be equal to the transmission from port 4 to 1, i.e. S_{14} , by reciprocity (see Equation (A.9) of Appendix A). Yet the latter has in turn to be equal to S_{32} if the symmetry along the z -axis is not also broken. Thus, with asymmetry along x yet mirror symmetry in z , the transmission still remains a symmetric function of k_x . This fact can also be observed in simulation as shown in Figure 2.8b. Adding a residual layer of thickness t below the nanobeams breaks the symmetry along the z -axis, and thereby provides the odd-symmetry system response required for odd-order differentiation. Simulations show that the thickness t provides control over the phase asymmetry (see Figure 2.8b).

2.4. OPTIMIZED TRANSFER FUNCTIONS AND NUMERICAL TESTS

Using the insight gained from the previous paragraph it is possible to design metasurfaces with specific transfer functions optimized for 1st- and 2nd-order spatial differentiation.

Figure 2.9a shows the simulated transmission amplitude $|S_{21}|$ and phase $\arg(S_{21})$ as a function of the in-plane wave vector k_x , normalized by the free space wavevector k_0 at the design wavelength $\lambda = 633$ nm for a metasurface composed of dielectric nanobeams (width $w = 182$ nm, height $h = 123$ nm, pitch $p = 250$ nm and refractive index $n = 4$ typical for Si). In this design, optimized to perform 2nd-order differentiation, the angular response is close in amplitude to the ideal parabolic shape. The phase response shows a variation of approximately 0.9π , deviating at high angles from the ideal constant phase response, but still providing a close-to-ideal second derivative response.

Our metasurface design has two key features that distinguish it from earlier designs [14–16]. First of all, the metasurface operational numerical aperture is large ($\text{NA} \approx 0.35$). This feature enables processing images with high spatial content and hence high resolution. Moreover, it allows for direct implementation into standard imaging systems with similar NA, for instance by placing the metasurface right in front of a charge-coupled device (CCD) detector array, without the need for additional imaging lenses. This is a major advance over previously explored spatial differentiation schemes that operate at an NA that is ≈ 25 times smaller than what we demonstrate here. Second, the transmission in our design reaches unity at large wavevectors, enabling close-to-ideal image transformation efficiency, significantly larger than earlier attempts at realizing image processing metasurfaces.

Next, we use the optimized transfer function to numerically test how well the ideal 2nd-order differentiation is approximated by our realistic metasurface design. To this end, some simple input functions (see Figure 2.9b-e) are discretized into 1000 pixels and

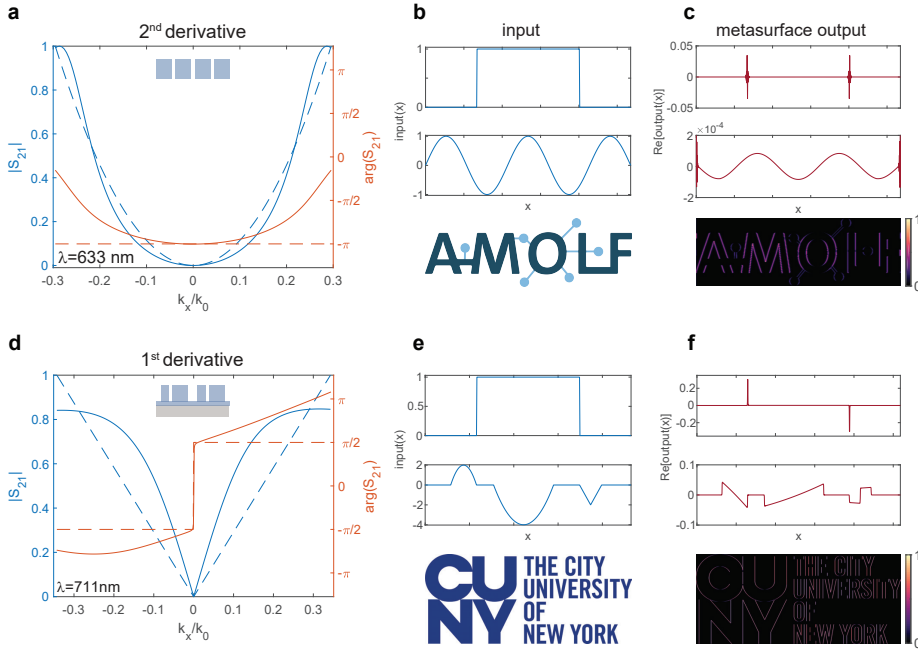


Figure 2.9: Simulated transfer functions of dielectric metasurfaces performing 1st- and 2nd-order spatial differentiation. **a** Transmission amplitude $|S_{21}|$ (solid blue line) and phase $\arg(S_{21}(k_x))$ (solid orange line) for the metasurface optimized for 2nd-derivative operation (sketched in the inset) at $\lambda = 633$ nm. The simulated transfer function is compared to the ideal case (dashed lines). The transmission reference plane is set such that the transmission phase at normal incidence equals $-\pi$. **b** Rectangular and sinusoidal input functions and 2D image that are used to numerically test the metasurface operation. The signal is discretized into 1000 pixels with individual pixel size set such that the Nyquist range matches the operational range in k -space of the metasurface. **c** Metasurface output for the input in **b**. For the 2D image, differentiation is performed line by line along the x -axis. **d-f** Same as **a-c**, but for 1st-derivative operation (metasurface geometry sketched in the inset) compared to the ideal case (dashed lines) at $\lambda = 711$ nm. The transmission reference plane is set such that the transmission phase at normal incidence is 0.

Fourier transformed. The pixel size Δ_x set such that the Nyquist frequency (i.e. the spatial sampling frequency) $\nu_n = 1/\Delta_x$ is equal to $k_{\max}/2\pi$ where k_{\max} is the maximum k_x -vector that the metasurface can process. This choice ensures that the Nyquist range $[-\nu_n, \nu_n]$ matches the operational range in k -space of the metasurface and physically means that the test images are projected onto the metasurface under an NA that matches that of the metasurface. Once the input function is Fourier transformed, it is multiplied by the transfer function and finally, inverse Fourier transformed (recall Eq. (2.4)).

Figure 2.9c shows the calculated response for rectangular and sinusoidal input functions shown in Figure 2.9b. The metasurface output clearly shows the edges of the rectangular input profile and flips the sinusoidal input function as expected. It is also possible to process arbitrary 2D images by performing the 2nd derivative line by line. The edges of one of our institutions' logos are clearly visible in Figure 2.9c. Notice that dif-

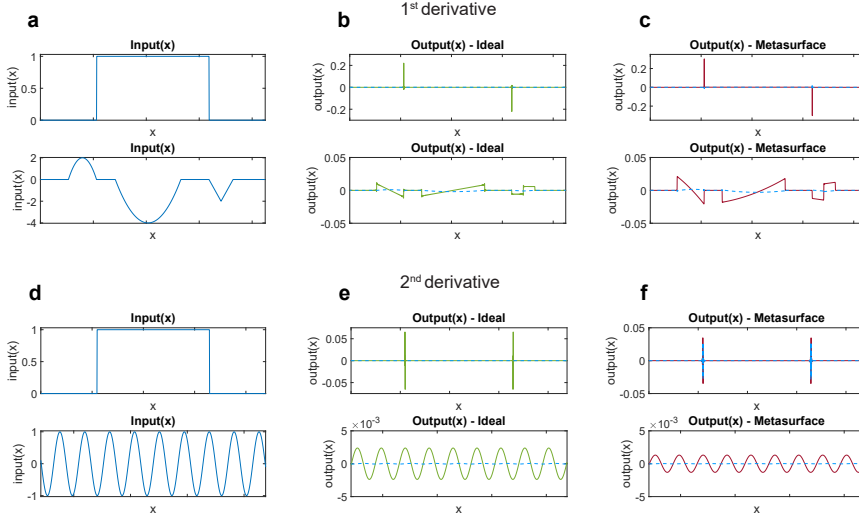


Figure 2.10: Metasurfaces performing 1st- and 2nd-order spatial differentiation. **a-d** Input functions used to numerically test the metasurface operation. The signal is discretized into 2048 pixels with individual pixel size set such that the Nyquist range matches the operational range in k -space of the metasurface. **b-e** Ideal output for the input in panels a-d. **c-f** Metasurface output for the input in panels a-d. The solid line represents the real part while the dashed line represents imaginary part of the output.

ferentiation is performed only along the x -axis for this 1D geometry, hence the edges along the same direction are not detected. To illustrate the flexibility of the metasurface image processing concept, Figure 2.9d shows the optimized transmission for a metasurface performing 1st-order differentiation, which corresponds to the transfer function $S_{21}(k_x) = ik_x$ in the Fourier domain. In order to achieve such an operation with odd symmetry in space, we designed an asymmetric metasurface composed of an array of Si nanobeams with a unit cell ($p = 300$ nm) consisting of nanobeams with two different widths ($w_1 = 48$ nm, $w_2 = 96$ nm, $h = 165$ nm and gap between the nanobeams 53 nm), placed on a thin silicon layer (thickness $t = 35$ nm) on a semi-infinite Al_2O_3 substrate. As explained earlier, by Lorentz reciprocity, it is easy to prove that the unit cell has to be asymmetric both along the direction of propagation and transversally. Furthermore, the asymmetry in the phase response of the transfer function can be tuned with t , enabling the required π phase jump at $k_x = 0$. In this case, the experimental optical constants (including losses) for the two materials have been used in the simulations [17, 18]. The simulated transfer function amplitude shows a linear behavior over a wavevector range up to $k_x/k_0 = 0.1$ (6°), above which it gradually bends away from the ideal case. For large angles, the transmission saturates below unity due to intrinsic absorption in Si. Figure 2.9e-f shows the calculated metasurface output for rectangular, parabolic and triangular input functions. The input slope changes and a nearly linear derivative for the parabola are clearly resolved. Furthermore, processing the logo results in clear detection of the edges in the x -direction consistently with 1st-derivative operation.

In order to further corroborate the performance of the designs, we compare the metasur-

face response to its ideal counterpart in Figure 2.10. It is easy to notice that the metasurfaces' output is very close to the ideal one both in real and imaginary part. The transfer functions used for the metasurface outputs are the same as in Figure 2.9a-d. Regarding the ideal differentiation, $S_{21} = ik_x$ and $S_{21} = -k_x^2$ were used as transfer functions for 1st- and 2nd-order derivative respectively.

To conclude, the results shown in this section demonstrate the possibility of designing metasurfaces featuring transfer functions that allow even- and odd-symmetric operations. These optimized designs are composed of nanostructures that can be realistically fabricated and experimentally tested, as shown in the next section.

2.5. FABRICATION

In order to demonstrate experimentally the concept of performing all–optically mathematical operations via metasurfaces, two different samples ought to be fabricated: the metasurface itself but also the image that is projected onto it. Both sample fabrication procedures involve electron beam lithography (EBL). This technique consists in scanning a focused electron beam on a surface coated with a layer of e-beam resist, a particular material that undergoes a change in solubility once exposed. Next, immersing the sample in a selective solvent will dissolve the exposed areas thus creating a mask for a successive etching that will eventually define the structure.

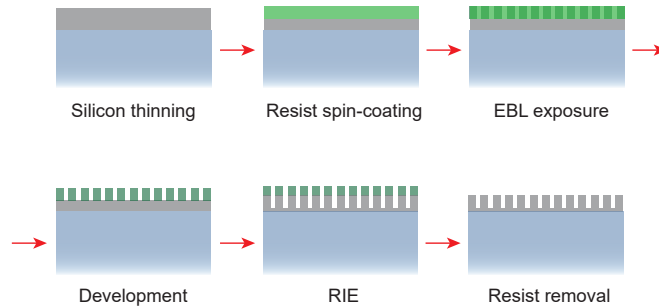


Figure 2.11: Fabrication steps needed for the metasurface sample.

Starting with the metasurface fabrication, we opted to fabricate the optimized geometry for 2nd–order differentiation as this symmetric structure is easier to obtain compared to the fully asymmetric one optimized for 1st–order differentiation.

The platform used for this sample is Silicon on sapphire (Al_2O_3). Indeed, high purity c-Si can be hetero-epitaxially grown on synthetic sapphire wafers and this CMOS technology is now well developed and commercially available. Using the experimental indices for the two materials [17, 18], the optimized dimensions for this design are $w = 206$ nm, $h = 142$ nm, and $p = 300$ nm with a thin residual Si layer (thickness $t = 20$ nm) that is intentionally left between the pillars. This layer is essential to achieve optimum transmission for large wavevectors, as discussed later. In the following, the detailed fabrication procedure is explained step by step.

- c-Si on Al_2O_3 substrates were purchased from MTI corp. The Si(100) layer is 500 nm–thick, polished (surface roughness < 2.5 nm) and undoped. The sapphire (orientation: R –plane) substrate is 0.46 mm–thick and double–side polished (surface roughness < 0.3 nm on the front side and optical grade polish on the back).
- The substrate was cleaned in base piranha and the c-Si was etched to the final metasurface thickness via Reactive Ion Etching (RIE) using Oxford Instrument’s PlasmaPro 100 Cobra ICP and a three–step process employing Cl_2 , HBr and O_2 . The first steps is used to remove the native oxide on the Si layer:

Cl ₂ gas flow	50 [sccm]
pressure	7 [mTorr]
Set temperature	60 [°C]
RIE forward power	30 [W]
ICP power	750 [W]
time	11 [s]

Next, the system is pumped out for 2 minutes in order to completely remove any residual Cl₂. The third step etches the Si layer:

HBr gas flow	48 [sccm]
O ₂ gas flow	2 [sccm]
pressure	7 [mTorr]
Set temperature	60 [°C]
RIE forward power	30 [W]
ICP power	750 [W]
time	89 [s]

The recipe is run first on a dummy wafer to condition the chamber and then on the actual sample. The etch rate of the entire process is $h_{\text{etched}}(t) = 45 \pm 18 + (3.7 \pm 0.24)t$ where h_{etched} is the etched thickness in [nm] and t is the Si-step etch time in [s] (the Cl₂ etch step time is kept constant and partially etches also Si). The final c-Si thickness is checked with Filmetrics F20, an optical characterization tool that fits the Fabry–Pérot sample spectrum to obtain the thickness.

This fabrication step is rather sensitive since the actual etch rate depends on the chamber conditions and on other poorly controllable parameters. Moreover, since the etch time is very long a small fluctuation on the etch rate can cause a relevant change in the final thickness.

- The substrate was cleaned again in base piranha and a 200 nm-thick layer of CSAR 62 (AR-P 6200, 9% in anisole) positive-tone resist (ALLRESIST GmbH) was spin-coated at 4000 rpm and baked for 2 minutes at 150°C.
- Lines were fabricated in the CSAR layer by exposure using a Raith Voyager lithography system (50 kV, dose 145–150 $\mu\text{C}/\text{cm}^2$) and development in Pentyl–acetate (60 s) and o–Xylene (10 s). One important detail concerning this step is that the nano-beams have to be aligned along the optical axis of sapphire during e-beam exposure. This is due to the fact that sapphire is a birefringent material and therefore has a refractive index that depends on the polarization impinging light. If the nanobeam arrays are aligned to the optical axis, light polarized along the wires length experiences only one refractive index.
- The pattern was then transferred into the c-Si by a three-step RIE process employing Cl₂, HBr and O₂. The latter is almost identical to that described previously except for the ratio between the fluence of O₂ and HBr gases. This has an influence on the slanting of the final structure sidewall and an optimum slanting of only 20 nm was achieved with 48.7 sccm for HBr and 1.4 sccm for O₂.

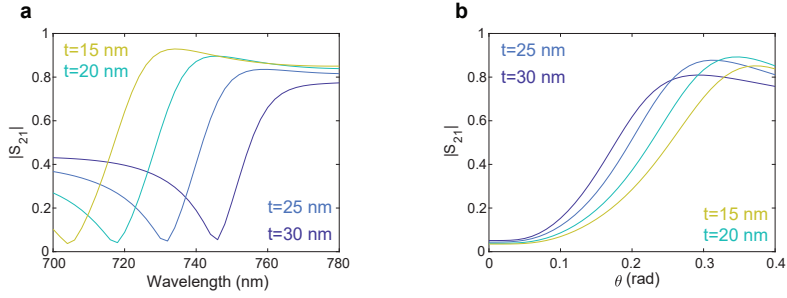


Figure 2.12: **a** Metasurface transmission spectrum for different residual thicknesses t . **b** Metasurface angular transmission $|S_{21}|$ at the wavelength of the minimum for different values of t

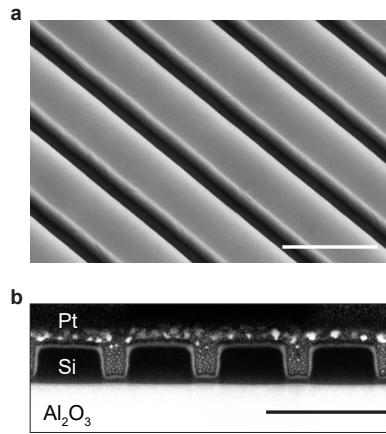


Figure 2.13: Experimental Si metasurface performing 2nd-order spatial differentiation. **a** Tilted SEM image of the Si metasurface performing the 2nd-derivative operation. **b** SEM image of a FIB cross section of the same metasurface showing the Si nanobeams (capped by Pt for imaging purposes) on an Al₂O₃ substrate. The scale bar is 400 nm for both panels.

Again, the etch time is an important parameter as it defines the residual thickness left in between the nanobeams. This, in turn, has an impact on the transmission spectra and the metasurface angular response, as shown in Figure 2.12. In fact, both the GMR and the Fabry–Pérot background are influenced by a change in the residual thickness t .

- The sample was finally cleaned in anisole at 65°C followed by an acid piranha cleaning.

Figure 2.13 shows the result of the fabrication procedure. The sample is uniform over large areas (500 μm) with very low sidewall roughness. The FIB cross-section in Figure 2.13b highlights the low sidewall slanting and the thin (thickness $t \approx 22$ nm) Si residual layer.

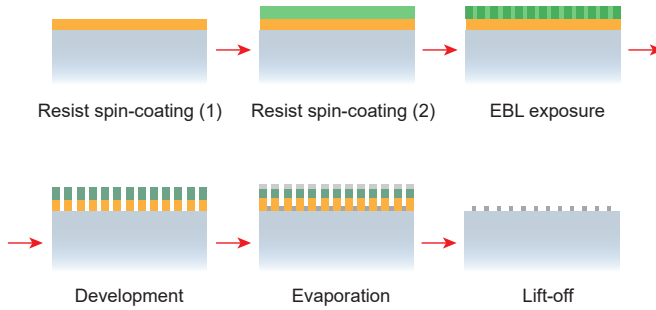


Figure 2.14: Fabrication steps needed for the images sample.

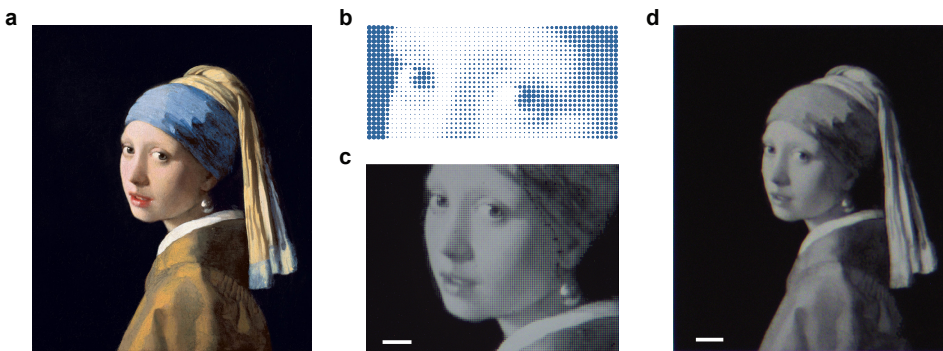


Figure 2.15: **a** *Meisje met de parel*, Johannes Vermeer circa 1665, oil on canvas, Mauritshuis, The Hague, Netherlands. **b** An array of suitably sized dots can imitate a gray-scale gradient. **c-d** Optical microscopy images of the final sample (scalebar 20 μm).

The fabrication procedure just described is an example of a top-down process in which a nanostructure is carved into a certain material. On the other hand, in order to fabricate the image samples, a bottom-up process is used, as schematically shown in Figure 2.14. The following steps were performed to fabricate the samples:

- Glass slides (24×24 mm) were cleaned in base piranha.
- A bilayer of MMA (MMA(8.5)MAA EL9, 150 nm) and PMMA (PMMA 950k A8, 95 nm) was spin-coated and baked at 150°C and 180°C for 2 minutes respectively. The thickness of the layers has to be chosen carefully, very thick layers would lift off easily in anisole but do not allow high resolution due to beam broadening during e-beam exposure and excessive MMA undercutting during development.
- The images were fabricated in the resist layer by exposure using Raith Voyager lithography system (50 kV, dose 550 $\mu\text{C}/\text{cm}^2$) and development in MIBK:IPA (1:3 for 90 s).

- A 40 nm thick Cr layer was evaporated using an in-house built thermal evaporator.
- The residual resist was lifted-off in anisole at 65°C facilitating the process with an ultra-sonicator.

Following this procedure, two-tone and gray-tone images were fabricated. To obtain the gradient effect in the gray-tone image, the famous painting *Meisje met de parel* (J. Vermeer, circa 1665) has been discretized into an array of suitably sized Cr disks. The final result looks homogeneous if low magnification ($< 60\times$) is used in a standard optical microscope (see Figure 2.15).

2.6. OPTICAL CHARACTERIZATION

The last experimental effort consists in characterizing optically the fabricated samples. First, the metasurface transfer function has to be measured. Second, the image processing capabilities are tested by projecting the image sample onto the metasurface. These two different measurements are performed with two different setups that will be described in the following, along with the corresponding results.

2.6.1. INTEGRATING SPHERE

To experimentally determine the transfer function of the metasurface we measure angle-resolved transmission spectra. The data was collected with a Spectra Pro 2300i spectrometer equipped with a Pixis 400 CCD. The sample was mounted on a rotating stage and illuminated with collimated white light from a SuperK EXTREME/FIANIUM super-continuum laser. The transmitted light was collected by an integrating sphere and sent to the spectrometer through a multimode fiber (Figure 2.16a). Light was polarized along the nanobeams' direction.

Figure 2.16b shows the measured transmittance ($T = |S_{21}|^2$) spectra as the incident angle is changed from 0 to 25°. In agreement with the simulated data in Figure 2.3, the Fano resonance shifts to shorter wavelengths as the angle is increased. The transmittance minimum is observed at $\lambda = 726$ nm for normal incidence and amounts to 2.2%, the residue attributed to minor fabrication imperfections. Figure 2.16c shows the transmittance as a function of the in-plane wavevector at $\lambda = 726$ nm, derived from the data in Figure 2.16b. The corresponding transmission amplitude ($|S_{21}|$) derived from the data is also plotted, along with the ideal parabolic amplitude response.

The overall trend with increasing transmittance as a function of angle is well reproduced experimentally, with a significant residual transmittance at normal incidence and a maximum amplitude at the largest angle of 0.84, which is mostly determined by the absorption in Si. Employing alternative high-index materials could further enhance the transmission for large angles.

2.6.2. DUIMELIJN FOURIER MICROSCOPE

In order to assess the processing capabilities of the metasurfaces, an image is projected onto the sample and the outcome is inspected on a CCD camera using the optical setup

Duimelijntje is a fairy tale by the danish writer Hans Christian Andersen (published in 1836) and also the name given to the setup.

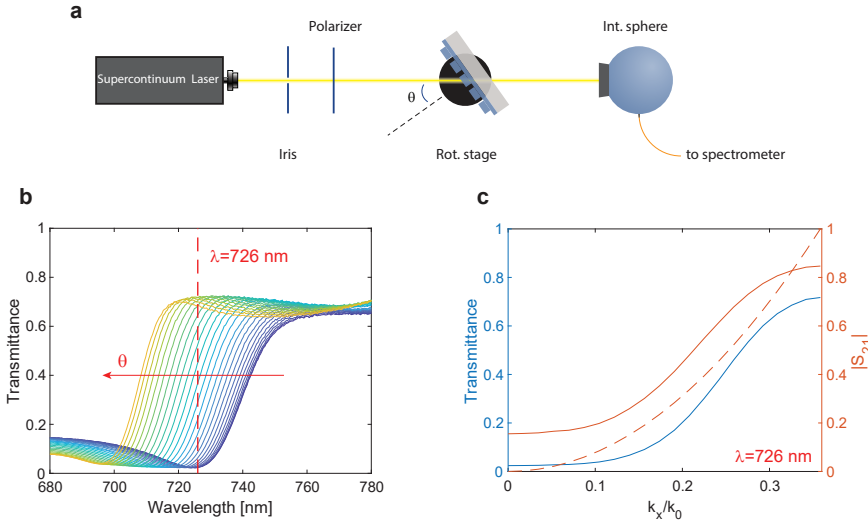


Figure 2.16: Experimental metasurface transmission. **a** Schematic of the setup used to measure angle-resolved transmission spectra. **b** Measured transmission spectra of the metasurface in Figure 2.13 as the angle of incidence is increased from 0 (blue line) to 25° (yellow line) in 25 steps. **c** Measured transmittance $|S_{21}|^2$ (blue line) and corresponding calculated transmission amplitude $|S_{21}|$ (orange solid line) as function of incident in-plane wave vector k_x/k_0 at $\lambda = 726$ nm. The dashed orange line shows the ideal parabolic transfer function for $|S_{21}|$.

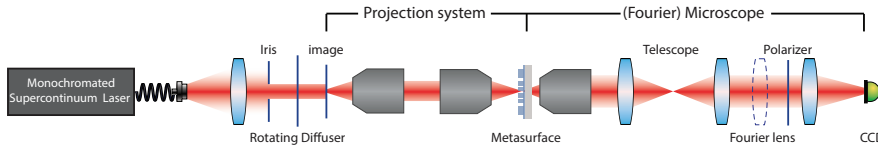


Figure 2.17: Projection system coupled to a standard microscope with Fourier imaging capabilities. The dashed contour represents the removable Bertrand lens.

in Figure 2.17. The illumination is provided by a SuperK EXTREME/FIANIUM supercontinuum white-light laser that is monochromated (1 nm bandwidth) by an Acousto-Optic Tunable Filter (AOTF) and subsequently coupled to a single-mode fiber. The output of the fiber is collimated by a condenser lens and passed through a spinning diffuser plate to evenly illuminate the image which is composed of Cr patterns on glass. The diffuser also serves to remove speckle artefacts in imaging that otherwise occur due to the large spatial coherence of the source. The image is projected at unity magnification onto the metasurface by two Olympus MPlanFL N 20x-0.45NA objectives. The second half of the setup is a standard microscope with Fourier imaging capabilities, already reported in Ref.[19]: the image is collected by either of two objectives (Nikon Plan Fluor 20× – 0.5 NA and Nikon S Plan Fluor ELWD 60× – 0.7 NA) and projected onto a Photometrics CoolSNAP EZ silicon CCD camera by a 20 cm focal distance tube lens. In between objective and tube lens, a 1:1 telescope provides an intermediate real space plane, while flipping in the Fourier (or Bertrand) lens allows projection of the back focal plane of the objective

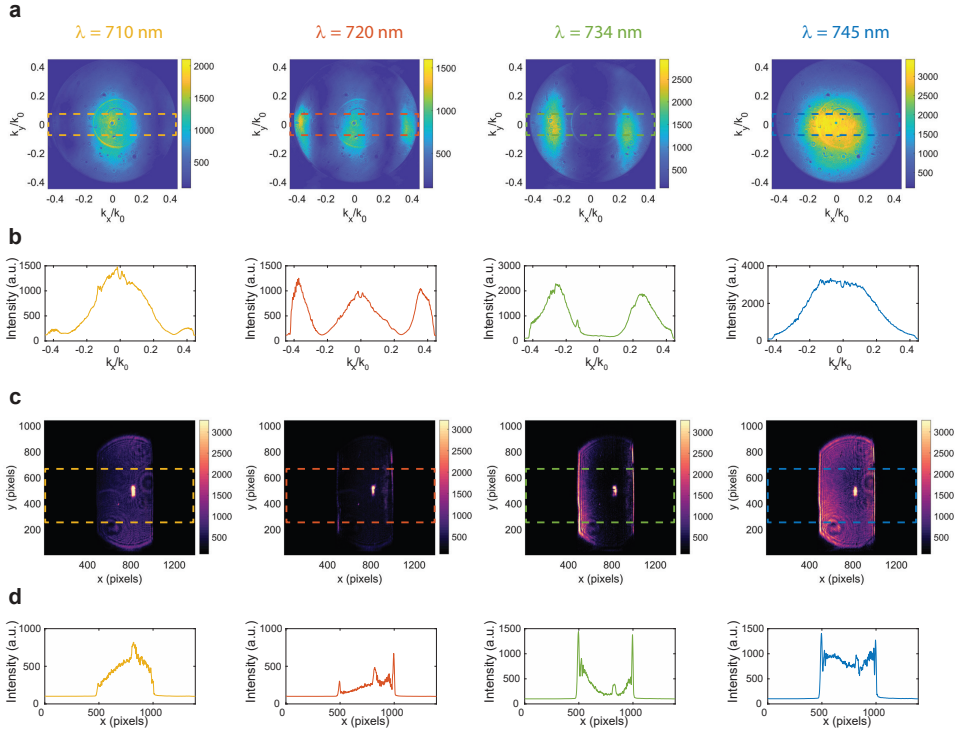


Figure 2.18: **a** Fourier space intensity map of light transmitted through the metasurface as the excitation wavelength is changed. **b** Average along the y -axis within the dashed box in **a**. **c** Image of the metasurface output as the excitation wavelength is changed. The input image is a slit. **d** Average along the y -axis within the dashed box in **c**.

directly onto the CCD [20] (Fourier imaging mode, unit magnification from back focal plane to objective).

This setup also allows transfer function amplitude measurements if the image and the first objective (from left) are removed and the Bertrand lens is flipped in. Indeed, using this configuration, light transmitted through the metasurface under a certain span of angles (dependent on the objectives' NA) is imaged in k -space and therefore the amplitude of the metasurface transfer function can also be obtained. However, compared to the simpler transmission setup described above, normalization of the intensity is more difficult and less reliable since it requires realignment and repositioning of the objectives. For this reason, while this technique is very insightful and gives information also for $k_y \neq 0$, it is still preferable to use the integrating sphere and a rotating stage to measure quantitatively the transfer function.

Figure 2.18a shows such not normalized transfer function amplitudes as the excitation wavelength is scanned across the resonance. The dark blue regions in these colormaps signal the spatial components that the metasurface is rejecting, either by absorption or

by reflection. As the wavelength is increased, the minima in k -space are moving closer to normal incidence ($\mathbf{k} = 0$): only on resonance it is possible to couple to the leaky mode from normal incidence, while for an off-resonant wavelength also an off-normal incident excitation is required, as expected from momentum matching. Furthermore, the transfer function is completely transforming in a narrow bandwidth going from a low-pass spatial filter ($\lambda = 710$ nm) to a high-pass spatial filter on resonance. At $\lambda = 745$ nm the metasurface is not imparting any modulation in k -space and the Gaussian profile of light out-coupling from the fiber and scattered evenly from the diffuser is retrieved.

These measurements clearly show the 1D nature of the metasurface operation. In fact, on resonance low k_x spatial components are suppressed also for a wide range of k_y . Hence, the 2nd-order differentiation is experimentally performed in a line-by-line fashion, in agreement with the numerical calculation shown in Figure 2.9 of Chapter 2.

Flipping out the Bertrand lens and inserting the first objective and an image, it is possible to study the metasurface image processing corresponding to the transfer functions just discussed (see Figure 2.18c). In this case the image is a simple adjustable slit. At $\lambda = 710$ nm the metasurface is acting as a low-pass filter so the image of the slit is blurred and the edges are smoothed. On resonance the edges are clearly detected while off-resonance, for $\lambda = 745$ nm, the image of the slit is recovered. The bright spot in Figure 2.18c is an artefact due to spurious reflection at the interface between air and the sapphire substrate.

Finally, we experimentally investigate the 2nd-derivative operation of the Si metasurface when more complex images are projected onto the sample. We first project the image of one of our institutions' logos onto the metasurface using off-resonant illumination ($\lambda = 750$ nm) and then image the metasurface output onto the CCD (Figure 2.19b); the contrast of the input object is clearly maintained. On the other hand, for resonant illumination at $\lambda = 726$ nm (Figure 2.19c) the edges are clearly resolved in the transformed image. As expected, no edge contrast is observed for features along the x -direction since the derivative operation is performed along the same direction.

To study the edge profile in a quantitative manner, Figure 2.19d (red curve) shows a line profile taken along the horizontal direction in the processed image (red dashed line in Figure 2.19c). These data are compared to the calculated output profile assuming an ideal parabolic transfer function (blue curve in Figure 2.19d). Overall the experimental and ideal response show very similar trends: the double-peaked structure expected for 2nd-order differentiation is clearly resolved in all of the six edges shown in Figure 2.19d. The discrepancies between experimental and ideal response are also probably due to a minor misalignment of the sample inducing small asymmetries in the transfer function.

Finally, we demonstrate the use of a Si metasurface for the processing of a gray-tone image of the *Meisje met de parel* described in the previous section. An off-resonant transmission image through the metasurface is shown in Figure 2.19f; the fine features and the contrast in the original object are clearly reproduced in the image. In contrast, the image processed at the resonant wavelength $\lambda = 726$ nm clearly shows the vertical edges along the face contour. The contours are fading away as they become gradually aligned with the x -axis, as expected. This clearly demonstrates that the metasurface image processing concept can be applied to more complex images containing gradients in transmission.

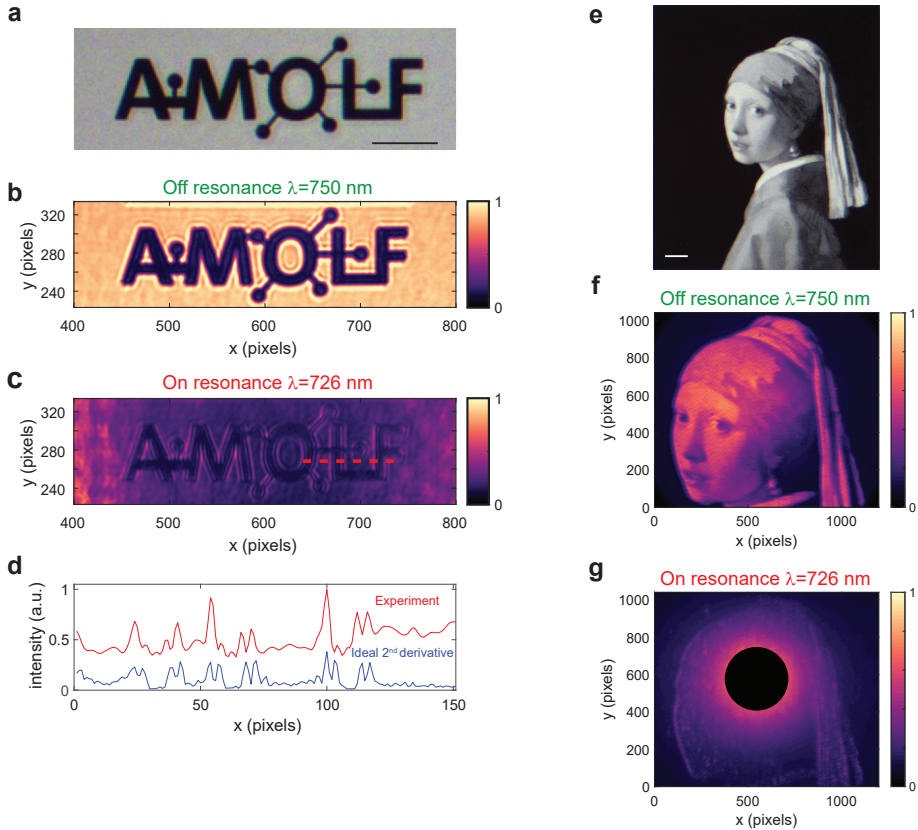


Figure 2.19: Experimental 2nd-order image differentiation. **a** Optical microscopy image of the input object; the scale bar is 20 μm **b-c** Optical microscopy image of the metasurface output for resonant ($\lambda = 726$ nm) and off-resonant ($\lambda = 750$ nm) illumination. **d** Cross-cut through **b** (red line) averaged over 8 pixels along y , compared to ideal differentiation performed on the off-resonant image (blue line). **e** Optical microscopy image of the *Meisje met de parel* (J. Vermeer, circa 1665). The image is composed of micron-sized dots of Cr on glass. **f-g** Metasurface output for resonant and off-resonant excitation. The black spot in **g** covers an artefact due to spurious reflection at the interface between air and the sapphire substrate.

2.7. 2D OPERATIONS AND UNPOLARIZED ILLUMINATION

The metasurface designs presented above are limited to 1D operation and work for light of a specific polarization. While this is an insightful proof-of-concept, designs that can perform 2D mathematical operations on impinging images independently of the polarization are essential for practical implementations. It is possible to achieve this by exploiting highly rotationally symmetric lattices: the designs are based on a triangular lattice of air holes carved into a suspended silicon membrane, which sustains a Fano resonance stemming from the coupling of a leaky-wave mode to a longitudinal Fabry-Pérot resonance, similar to the design concept explained above.

Extending the formalism used so far, consider a linearly polarized beam impinging on our metasurface, corresponding to an arbitrary 2D image, with a transverse field profile

$$\mathbf{E}_{x,y}^{\text{in}}(x, y) = \begin{pmatrix} E_x^{\text{in}}(x, y) \\ E_y^{\text{in}}(x, y) \end{pmatrix} \quad (2.11)$$

where the subscript x and y indicate the x - and y -polarized field components. Upon interaction with the metasurface, the input beam is filtered in momentum space (k -space) by the 2×2 transmission tensor S of the metasurface (i.e. transfer function)

$$S_{21} = \begin{pmatrix} S_{ss}(k_x, k_y) & S_{sp}(k_x, k_y) \\ S_{ps}(k_x, k_y) & S_{pp}(k_x, k_y) \end{pmatrix} \quad (2.12)$$

where S_{uv} is the transmission coefficient from an input v -polarized wave to an output u -polarized one with transverse wavevector $\mathbf{k}_{\parallel} = k_x \hat{\mathbf{x}} + k_y \hat{\mathbf{y}}$.

The output signal is calculated as follows. The input signal is Fourier-transformed $\mathcal{F}[\mathbf{E}_{x,y}^{\text{in}}(x, y)]$ and converted into the sp -polarization basis via multiplication with the matrix

$$\mathbf{R} = \begin{pmatrix} \sin \phi & \cos \phi \\ -\cos \phi & \sin \phi \end{pmatrix} \quad (2.13)$$

where ϕ is the azimuthal angle between \mathbf{k}_{\parallel} and the x -axis. This spectrum is filtered by the metasurface transfer function S and projected back onto the xy -polarization basis by multiplying it with \mathbf{R}^{-1} . Finally, an inverse Fourier transform is performed to derive the spatial profile of the output field. These steps are captured in the following equation for the transmitted image $\mathbf{E}_{x,y}^{\text{out}}(x, y)$

$$\begin{pmatrix} E_x^{\text{out}}(x, y) \\ E_y^{\text{out}}(x, y) \end{pmatrix} = \mathcal{F}^{-1} \left[\mathbf{R}^{-1} \begin{pmatrix} S_{ss}(k_x, k_y) & S_{sp}(k_x, k_y) \\ S_{ps}(k_x, k_y) & S_{pp}(k_x, k_y) \end{pmatrix} \mathbf{R} \left(\mathcal{F} \left[\begin{pmatrix} E_x^{\text{in}}(x, y) \\ E_y^{\text{in}}(x, y) \end{pmatrix} \right] \right) \right] \quad (2.14)$$

Within this formalism, it is possible to calculate the response for unpolarized light assuming that the input field is constituted by both x - and y -components with the same intensity and random phases. Then, the average intensity of detected light is found by adding the intensities of the two orthogonal polarization components.

Ideally, the metasurface should have identical response to both polarizations, and have no polarization mixing in its response function. Thus the transfer function in Eq.(2.12) should be of the form $S_{21} = S(k_x, k_y) \mathbb{I}_2$, where $S(k_x, k_y)$ is an arbitrary scalar function and \mathbb{I}_2 is the 2×2 identity matrix. Next, if the response is also azimuthally symmetric,

$S(k_x, k_y) = S(k_{\parallel})$, with $k_{\parallel} = (k_x^2 + k_y^2)^{1/2} = k_0 \sin \theta$ and θ is the incidence angle with respect to the normal direction to the metasurface.

Focusing on the case of differentiation, azimuthal symmetry is only possible for even-order operations, in which case $S_n(k_{\parallel}) = A_n (i k_{\parallel})^n$, where n is the differentiation order and A_n is a constant. For example, in the case of second-order differentiation, the response corresponding to the Laplace operator $\nabla^2 = \frac{\partial^2}{\partial x^2} + \frac{\partial^2}{\partial y^2}$ is²

$$S_2(k_x, k_y) = \begin{pmatrix} A_2(k_x^2 + k_y^2) & 0 \\ 0 & A_2(k_x^2 + k_y^2) \end{pmatrix} = A_2(k_{\parallel})^2 \mathbb{I}_2 \quad (2.15)$$

Interestingly, azimuthal symmetry is not possible for odd-order differentiation. For this type of operations, $S(k_x, k_y)$ can be defined along a radial direction as $S_n(k_x, k_y) = A_n(\phi) (i k_{\parallel})^n$, where $A_n(\phi)$ is a function of the azimuthal angle. As an example, the first-order differentiation is described through

$$S_1(k_x, k_y) = A_1(\phi) (i k_{\parallel}) \mathbb{I}_2 \quad (2.16)$$

and involves a π phase jump with respect to $\theta = 0$ (normal incidence). As shown earlier, implementing such an operation requires metasurfaces breaking symmetries in both transverse and longitudinal directions.

Following the design principles explained in Section 2.3, it is possible to engineer the metasurfaces' response in transmission. Starting with the case of 2nd-order differentiation, the metasurface consists of a triangular array of air holes (lattice constant a and radius r) carved in a thin Si membrane of thickness t (see Figure 2.20a). The high rotational symmetry of the lattice implies polarization insensitivity at normal incidence,³ and a quasi-isotropic response in ϕ over the entire transverse momentum space.

The optimal metasurface parameters for second-order spatial differentiation at $\lambda = 717$ nm are $a = 250$ nm, $r = 120$ nm, and $t = 125$ nm. Figure 2.20b-c, shows the transmission amplitude for the co-polarized components of the transmission matrix. Cross-polarized transmission amplitudes are negligible (data shown in the Supporting Information of Ref. [22]). The design and simulations consider realistic material loss [23], which limits the maximum achievable transmission to ~ 0.7 . Both amplitude and phase responses are symmetric in all transverse directions, as required for ideal even-order differential operation. Furthermore, the metasurface supports an angular bandwidth of 8° for both s- and p-polarized illuminations, hence, allowing efficient 2D edge detection with $\text{NA} \approx 0.14$. It is worth comparing this design to the photonic crystal slab Laplace operator proposed by Guo et al. [14, 15]. While their design achieves a more isotropic response, the NA of operation is almost one order of magnitude smaller than what is presented here. This has an impact on the resolution and on the applicability of the structure to standard imaging systems that have typically larger NA. On the other hand, a non-perfectly isotropic response does not hinder edge-detection. Indeed, in order to as-

²The one-dimensional proof in Section 2.1 can be readily generalized to two dimensions. Similarly, partial differentiation in real space $\frac{\partial f(x,y)}{\partial x}$ corresponds to $i k_x F(k_x, k_y)$ in k-space. Other differential operators can be constructed in the same way (e.g. $\left(\frac{\partial^2}{\partial x^2} + \frac{\partial^2}{\partial y^2}\right) f(x, y) \rightarrow -(k_x^2 + k_y^2) F(k_x, k_y)$) [21].

³Any in-plane polarization vector can be written as a linear combination of two basis vectors that span the entire plane and for which the response is the same by symmetry (the same consideration applies in Chapter 5).

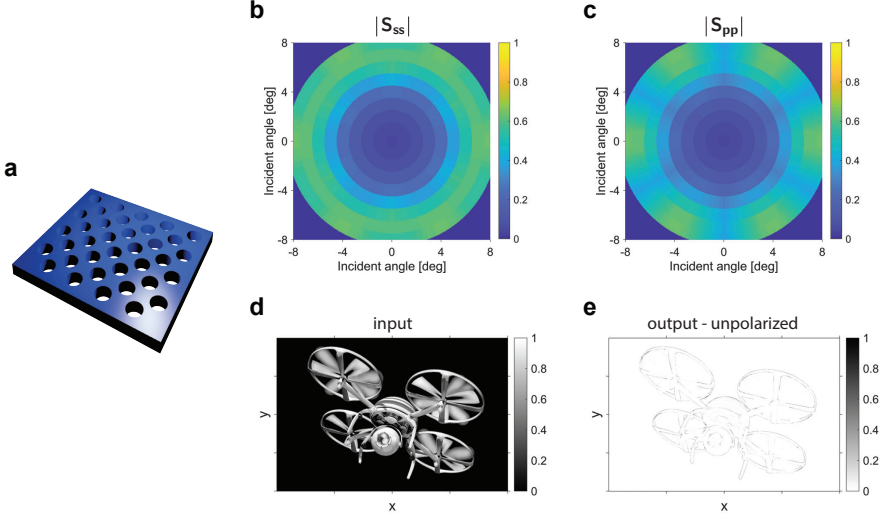


Figure 2.20: **a** 3D rendering of the proposed metasurface performing 2nd-order differentiation: a triangular array of air holes (lattice constant a and radius r) carved in a thin Si membrane of thickness t . **b-c** Transmission amplitude of co-polarized fields for the optimal design including Si losses. **d** 2D input image used to test the metasurface's edge detection functionality. **e** Metasurface output for the unpolarized input image in panel d.

to assess the functionality of the metasurface, the 2D input image in Figure 2.20d is projected onto the metasurface and the output is calculated through Eq.(2.14). The metasurface detects edges in all transverse directions with high efficiency for unpolarized illumination, as shown in Figure 2.20e. Overall, the metasurface response is very close to the ideal output from a second order (Laplacian) operation (data shown in Ref. [22]).

In order to implement odd-order differentiation, the transmission phase needs to be an odd function of the incidence angle θ , which requires breaking both transverse and longitudinal symmetries in the metasurface. To this end, our unit cell is modified as shown in Figure 2.21a, adding a thin SiO₂ substrate to break longitudinal symmetry (the symmetry parallel to the z -axis) and three small holes symmetrically distributed around the main hole to break transverse symmetry (the symmetry on the xy -plane). The transmission amplitude and phase for co-polarized fields is shown in Figure 2.21b-c. The metasurface exhibits an odd-order response along any radial direction, but it lacks rotational symmetry as in even-order differentiation. The metasurface achieves a near- π phase jump between the negative and positive transverse propagation momentum, which enables first-order differential operation at $\lambda = 628$ nm. Cross-polarized transmission is again negligible (data shown in the Supporting Information of Ref. [22]) and the metasurface performs differentiation with a NA ≈ 0.21 and ≈ 0.14 for s- and p-polarizations, respectively. The metasurface design parameters are $a = 300$ nm, $r = 130$ nm, $r_1 = 77$ nm, $t_{\text{sub}} = 50$ nm, $t_{\text{etch}} = 90$ nm, and the material is assumed lossless in this calculation, considering only the real part of the Si dispersive refractive index.

Again, it is important to explore the effect of the first-order differentiator metasurface

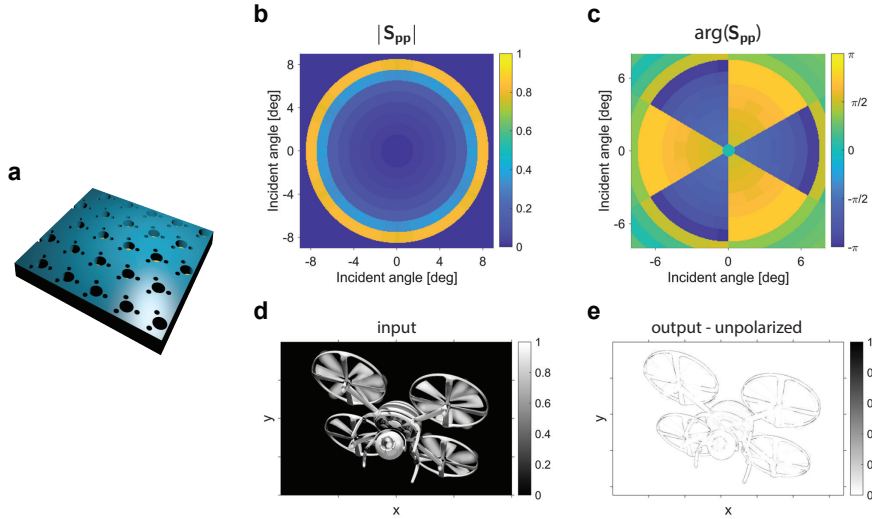


Figure 2.21: **a** 3D rendering of the proposed metasurface performing 1st-order differentiation. Extra air holes are added to the thin Si membrane design performing the Laplacian operator along with a SiO₂ thin layer. **b-c** Transmission amplitude (b) and phase (c) for co-polarized fields for the optimal design. **d** 2D input image used to test the metasurface's edge detection functionality. **e** Metasurface output for the unpolarized input image in panel d.

on the 2D input image in Figure 2.21d for different polarizations. The metasurface output demonstrates clear edge detection in all directions, highlighting all boundaries of the object for unpolarized illumination, even with a small difference of NA between s- and p-polarizations. Differences on 2D edge detection between the first- and the second-order differentiators are compared and provided in Ref. [22], showing that the first-order differentiator gives one peak per edge while the second-order counterpart results in a doubly-peaked structure as the one in Figure 2.19.

Even in the presence of some nonidealities, such as non perfectly isotropic response and polarization-dependent NA, the proposed designs can be realistically fabricated and reliably perform isotropic 2D optical image processing regardless of the illumination's polarization.

2.8. CONCLUSION

To conclude, this chapter introduces how dielectric metasurfaces sustaining Fano resonances with suitably engineered dispersion can perform mathematical operations on arbitrary 2D input signals, with immediate applications in image processing and edge detection.

First, the Fourier optics concepts needed throughout the chapter are briefly reviewed and explained. Next, the idea of using a metasurface sustaining a Fano resonance is elaborated along with the rationale used to design its angle-dependent transmission by tuning a few structural parameters. Moreover, the necessity of breaking the structure's

symmetry to engineer odd-order differentiation is elucidated. Using these insights, the ideal amplitude and phase transfer functions can be approximated over a relatively wide k -space range spanning a numerical aperture up to 0.35 and that transmission over 0.8 can be achieved for large angles. The optimized designs are numerically tested on input images and functions, demonstrating strong consistency with 1st- and 2nd-order differentiation.

The optimal design for 2nd-order differentiation is realized and the fabrication steps are discussed in detail. The finalized sample is characterized and its transfer function is measured. Finally, the metasurface image processing capabilities are experimentally demonstrated. We show clear edge detection at the resonant illumination $\lambda = 726$ nm as a result of the second-order spatial differentiation, both on high contrast and gray-scale projected images.

The last section extends these concepts to 2D operations and unpolarized illumination, enabling reliable detection of edges regardless of their orientation. Furthermore, it is worth mentioning that image processing metasurfaces were designed also in the microwave wavelength range using similar concepts yet exploiting different resonances [24].

Altogether, the results shown in this chapter can lead to a wide range of applications and can readily be implemented by directly placing the metasurface onto a standard CCD or CMOS detector chip, opening new opportunities in hybrid optical and electronic computing that operates at low cost, low power, and small dimensions.

REFERENCES

- [1] B. E. A. Saleh and M. C. Teich, *Fundamentals of Photonics*, Wiley Series in Pure and Applied Optics (Wiley, 2007).
- [2] J. W. Goodman, *Introduction to Fourier Optics*, 4th ed. (W. H. Freeman, 2017).
- [3] S. Fan and J. D. Joannopoulos, *Analysis of guided resonances in photonic crystal slabs*, Physical Review B **65**, 235112 (2002).
- [4] G. Pitruzzello and T. F. Krauss, *Photonic crystal resonances for sensing and imaging*, Journal of Optics **20**, 073004 (2018).
- [5] S. S. Wang and R. Magnusson, *Theory and applications of guided-mode resonance filters*, Applied Optics **32**, 2606 (1993).
- [6] S. S. Wang, M. G. Moharam, R. Magnusson, and J. S. Bagby, *Guided-mode resonances in planar dielectric-layer diffraction gratings*, Journal of the Optical Society of America A **7**, 1470 (1990).
- [7] B. Luk'yanchuk, N. I. Zheludev, S. A. Maier, N. J. Halas, P. Nordlander, H. Giessen, and C. T. Chong, *The Fano resonance in plasmonic nanostructures and metamaterials*, Nature Materials **9**, 707 (2010).
- [8] A. E. Miroshnichenko, S. Flach, and Y. S. Kivshar, *Fano resonances in nanoscale structures*, Reviews of Modern Physics **82**, 2257 (2010).
- [9] L. Andreani and M. Agio, *Photonic bands and gap maps in a photonic crystal slab*, IEEE Journal of Quantum Electronics **38**, 891 (2002).
- [10] U. Fano, *Sullo spettro di assorbimento dei gas nobili presso il limite dello spettro d'arco*, Il Nuovo Cimento **12**, 154 (1935).
- [11] S. Fan, W. Suh, and J. D. Joannopoulos, *Temporal coupled-mode theory for the fano resonance in optical resonators*, Journal of the Optical Society of America. A **20**, 569 (2003).
- [12] H. A. Haus, *Waves and fields in optoelectronics* (Prentice-Hall, Englewood Cliffs, N.J, 1984) p. 402.
- [13] D. L. Brundrett, E. N. Glytsis, and T. K. Gaylord, *Homogeneous layer models for high-spatial-frequency dielectric surface-relief gratings: conical diffraction and antireflection designs*, Applied Optics **33**, 2695 (1994).
- [14] C. Guo, M. Xiao, M. Minkov, Y. Shi, and S. Fan, *Isotropic wavevector domain image filters by a photonic crystal slab device*, Journal of the Optical Society of America A **35**, 1685 (2018).
- [15] C. Guo, M. Xiao, M. Minkov, Y. Shi, and S. Fan, *Photonic crystal slab Laplace operator for image differentiation*, Optica **5**, 251 (2018).

- [16] T. Zhu, Y. Zhou, Y. Lou, H. Ye, M. Qiu, Z. Ruan, and S. Fan, *Plasmonic computing of spatial differentiation*, *Nature Communications* **8**, 15391 (2017).
- [17] M. A. Green, *Self-consistent optical parameters of intrinsic silicon at 300K including temperature coefficients*, *Solar Energy Materials and Solar Cells* **92**, 1305 (2008).
- [18] I. H. Malitson and M. J. Dodge, *Refractive Index and Birefringence of Synthetic Sapphire*, in *Program of the 1972 Annual Meeting of the Optical Society of America*, Vol. 62 (1972) p. 1336.
- [19] I. Sersic, C. Tuambilangana, and A. Femius Koenderink, *Fourier microscopy of single plasmonic scatterers*, *New Journal of Physics* **13**, 083019 (2011).
- [20] J. A. Kurvits, M. Jiang, and R. Zia, *Comparative analysis of imaging configurations and objectives for Fourier microscopy*, *Journal of the Optical Society of America A* **32**, 2082 (2015).
- [21] R. N. Bracewell, *Relatives of the fourier transform*, in *The Fourier transform and its applications* (McGraw-Hill New York, 1986) pp. 329–335.
- [22] H. Kwon, A. Cordaro, D. Sounas, A. Polman, and A. Alù, *Dual-polarization analog 2D image processing with nonlocal metasurfaces*, *ACS Photonics* **7**, 1799 (2020).
- [23] E. D. Palik, *Handbook of Optical Constants of Solids* (Academic Press, Boston, 1998).
- [24] H. Kwon, D. Sounas, A. Cordaro, A. Polman, and A. Alù, *Nonlocal Metasurfaces for Optical Signal Processing*, *Physical Review Letters* **121**, 173004 (2018).